Journal of Wood Science

ORIGINAL ARTICLE

Experimental and nonlinear finite-element analysis study on lateral push resistance of San-dou components perpendicular and parallel to grain in traditional timber buildings

Chengwen Zhang, Qing Chun*, Yijie Lin, Haoyu Wang and Pan Li

Abstract

Dou-gong is an essential part of traditional timber buildings in East Asia, having a decoration function and a load transfer function. The San-dou component, which is vulnerable to the lateral push force of the Gong, Fang, and purlin, is a critical structural component in the Dou-gong. In San-dou components, there are two distinctive types of surfaces subjected to lateral push force, perpendicular to the grain and parallel to the grain. However, few investigation into the structural performance of these two types has been done. Considering this shortcoming in the literature, in the current study, tests were carried out to obtain elasticity and strength characteristics on 90 timber specimens of fir and larch. After the material property test, 24 San-dou specimens were prepared to investigate the lateral push resistance. Consequently, an elastic–plastic damage assessment model was developed to calculate the load–displacement curve and possible damage distribution region of San-dou component, using the nonlinear finite-element analysis. According to the analyses, the failure mode for the San-dou component perpendicular to the grain is a horizontal crack parallel to the Dou-ear. Besides, the failure mode of the San-dou component parallel to the grain is an oblique crack, which begins from the inner edge of the Dou-ear to the lower part of the San-dou component. In the case of the other factors being the same, the bearing capacity of the larch San-dou component is 49.64–55.78% stronger than the fir San-dou component. Besides that, the bearing capacity of the San-dou component perpendicular to the grain is 32.85–38.22% higher than the San-dou component parallel to the grain. The research findings are expected to give a theoretical foundation for the structural evaluation of the Dou-gong system in traditional timber buildings and a scientific basis for elucidating the differences in the construction of traditional timber buildings in East Asia.

Keywords: Ancient architecture, Traditional timber buildings, Elastoplastic damage, Nonlinear finite element, Lateral push resistance

Introduction

Dou-gong, a traditional symbol and vital element of Asian traditional timber constructions, has an aesthetic impact and serves as a vertical force transmission and lateral push resistance element [1]. Dou-gong is a type of complex timber structure with a variety of distinct components. The San-dou component is a critical structural bearing block that supports the upper Gong, beam, and purlin. The San-dou component is vulnerable to lateral push force resulting from the upper Gong, beam, and purlin. As depicted in Fig. 1, the cracking or breaking

*Correspondence: cqnj1979@163.com

School of Architecture, Southeast University, Nanjing 210096, China

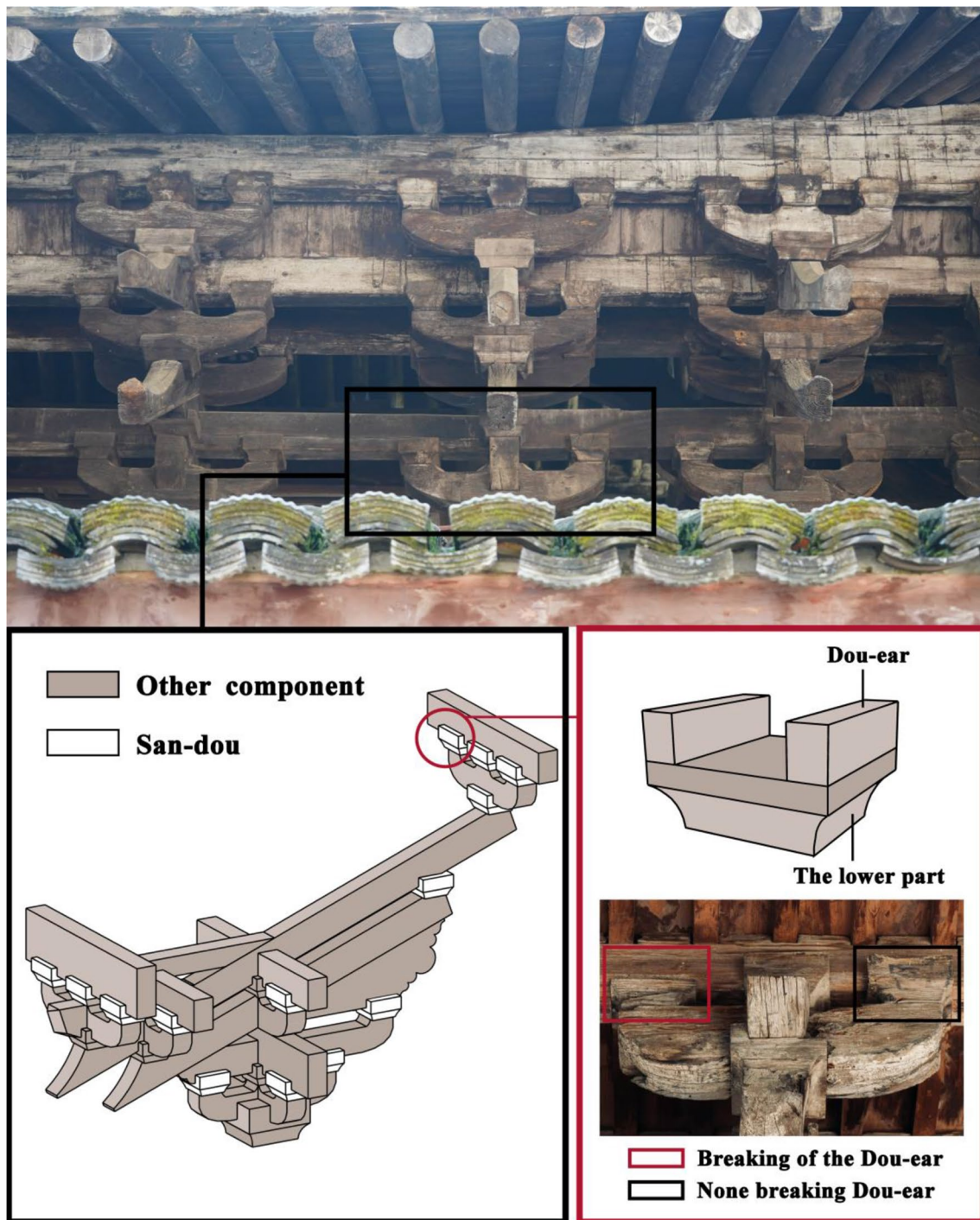Zhang *et al. Journal of Wood Science*   (2022) 68:41

Page 2 of 18

Fig. 1 Damage of San-dou component in Dou-gong

of the Dou-ear in San-dou component is a commonly occurred situation in practical timber buildings [2]. Therefore, examination of the lateral push resistance of the San-dou component in detail is a vital situation that needs to be performed immediately.

Based on the timber grain orientation aligning with respect to the beam direction, there are generally two types of placements for the San-dou component in the Dou-gong systems, according to the following investigation results of typical traditional timber buildings in East

Zhang *et al. Journal of Wood Science*   (2022) 68:41

Page 3 of 18

Asia. The first type is when the traverse surface of the timber grain of San-dou component is placed perpendicular to the beam direction (SDPP; Fig. 2a), while the second type is when the traverse surface of the timber grain of San-dou component is placed parallel to the beam direction (SDPL; Fig. 2b). The SDPL was widely utilized in Japan's Gangoji and China's Foguang Temple, as presented in Figs. 3 and 4. The SDPP has also been employed in Japan's Todaiji and China's Baoguo Temple.

In this paper, the San-dou components, in Chinese traditional timber buildings were chosen as study examples. For this purpose, a detailed site investigation of
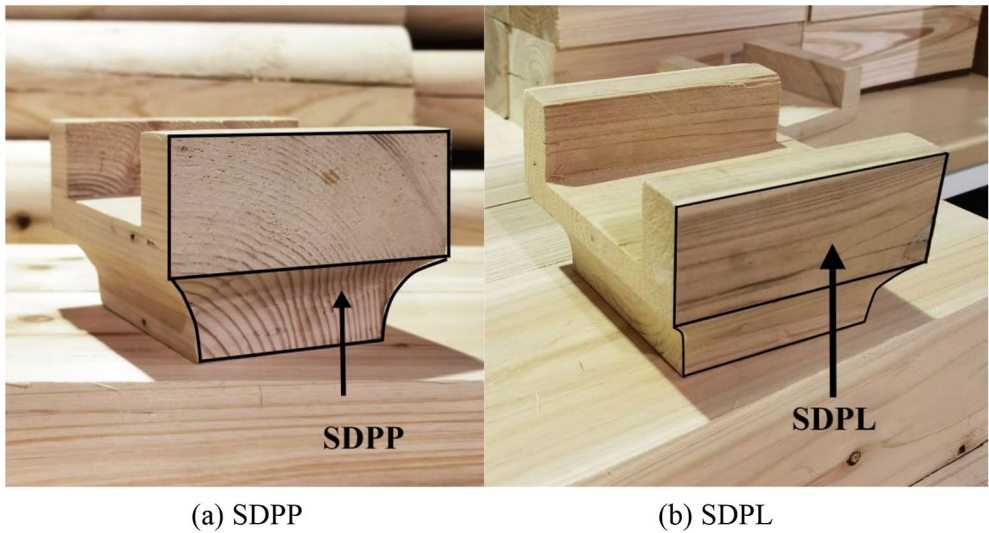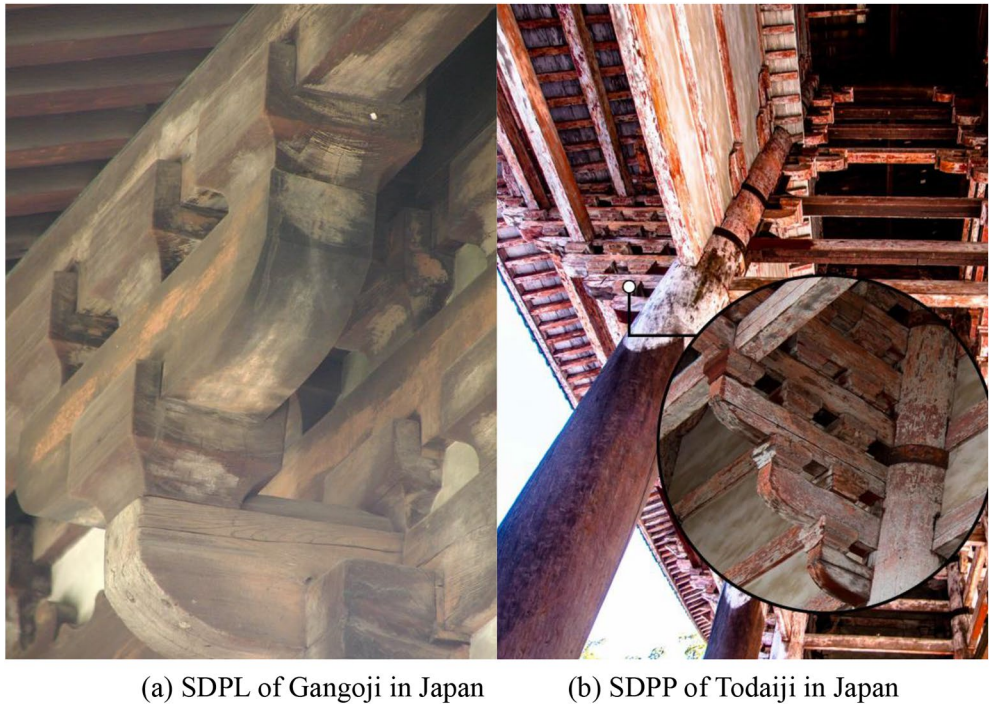

(a) SDPP   (b) SDPL

Fig. 2 Schematic diagram of SDPP and SDPL

(a) SDPL of Gangoji in Japan   (b) SDPP of Todaiji in Japan

Fig. 3 San-dou components commonly found in the traditional Japanese timber building

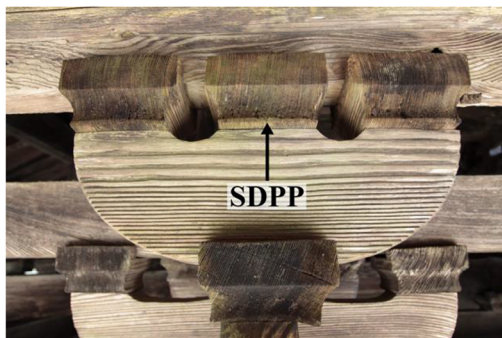Zhang *et al. Journal of Wood Science*　(2022) 68:41

Page 4 of 18

(a) SDPL of Jinci Temple Hall in northern China

(b) SDPL of Buddhist Temple Hall in northern China

(c) SDPL of Baoguo Temple Hall in southern China

(d) SDPL of Shisi Temple Hall in southern China

Fig. 4 San-dou components commonly found in the traditional Chinese timber building

four typical traditional timber buildings found in both northern and southern China was created in this paper. The results elucidate that traditional timber buildings in North China primarily employ SDPL, whereas traditional timber buildings in south China mainly use SDPP. The findings reflect the difference in the construction technology of traditional timber buildings between northern and southern China. For example, San-dou components in Jinci Temple Hall and Buddhist Temple Hall in North China are almost entirely SDPL, as shown in Fig. 4a, b. On the other hand, the SDPP is widespread in the Baoguo Temple Hall and Shisi Temple Hall in south China, as shown in Fig. 4c, d. The existing literature [3] also verifies the research results. Zhang Shiqing [3] points to the fact that "The machining process is the secondary effects for ancient craftsmen to choose SDPL or SDPP." Therefore, the motivation of this paper is to try to explain the difference between SDPP and SDPP in traditional timber buildings from the perspective of experimental research and nonlinear finite-element analysis.

Most studies on the San-dou components in the Dougong structures assume that the timber grain direction of the San-dou component was placed parallel to the beam direction [4–7], and the influence of the timber grain direction on the mechanical properties of San-dou component has seldom been investigated. At this point, only Zhou Miao [8] and Zhang Shiqing [3] investigated the timber grain orientation of San-dou component in traditional timber buildings, and the decoration and preparation process parameters were integrated into the investigation without structural analysis. However, several scholars have conducted significant research on timber grain orientation of the other geometric types of timber members [9–12], which may serve as a source of inspiration for the test methods and numerical analysis method used in this paper. According to the research conducted by the editorial team of the "Technical code for maintenance and strengthening of ancient timber buildings" [13], the main wood species used in traditional Chinese timber frame systems are larch, pine and fir. Moreover, the mechanical properties of wood parallel to grain were also tested [13]. The mechanical properties of the Japanese complex Dou-gong system were researched using static horizontal loading and shaking table test by Fujita et al. [14, 15], and the effect of wood grain direction on structural stiffness was investigated. Yeo et al. [16, 17] proposed a mechanical model for Dieh-Dou timber structures considering the effect of the wood grain direction, which provided high consistency with the experiment results. Yinlan et al. [18] and Wang et al. [19] simplified the timber beam or material specimens as an orthotropic model using the nonlinear finite-element method of elastic–plastic damage, considering the

Zhang *et al. Journal of Wood Science*   (2022) 68:41

Page 5 of 18

variations in three-dimensional material properties of timber. Xue et al. [20] used the three-dimensional elastic–plastic finite-element method to perform a parameter analysis for the vertical compressive performance of Dou-gong made from Korean pine. Qin and Yang [21] investigated the material properties of aged and new Tibetan Populus cathayana. Yang and Zhang [22] studied the material properties of new Korean Pine. Nairn [23] implemented the finite-element method to simulate cross-sectional grain orientation in early and late timber caused by different cutting procedures. In the study conducted by Mendis et al. [24] on the statistical analysis of timber cutting patterns in Sri Lanka's architectural heritage, it was found that there are many components such as timber beams or columns that are found to be subjected to stress parallel and perpendicular to the grain direction. Guindos [25] proposed a method to calculate the fiber orientation and basic mechanical properties of softwood using an integral calculation method. Chen et al. [26] established a temperature-dependent three-dimensional anisotropic plastic damage constitutive model for the numerical simulation of timber-based materials and connections.

To summarize clearly, the present study addresses the following issues lacking in the literature: (1) there are limited studies on SDPP and SDPL that only focus on architectural shapes and construction techniques. (2) In the present study, the numerical simulation and experimental design of the Dou-gong are all carried out using SDPL, and there is little research on the SDPP. (3) Most of the experimental studies available on Dou-gong grain focus on pine and larch, while studies focusing on fir remain limited. Moreover, few studies compare these types of timber commonly used in traditional Chinese timber buildings. Based on these factors, in the present study, 90 timber samples were designed and produced in the first stage, and then the material properties of larch and fir were tested to provide a basis for numerical simulation. In the second stage, 24 San-dou specimens from larch and fir were designed and produced to examine the lateral push resistance of SDPP and SDPL. Finally, the performance evaluations of SDPP and SDPL are investigated based on the elastic–plastic damage model.

Materials and tests
Timbers
The current study was carried out using Larch (*Larix gmelinii*) and Fir (*Cunninghamia lanceolate*) samples. The timber splitting method performed in 3 different directions along the grain, including longitudinal (L), radial (R), and tangential (T), is presented in Fig. 5. The material property tests included characteristics as follows: the tensile and compressive strength of wood
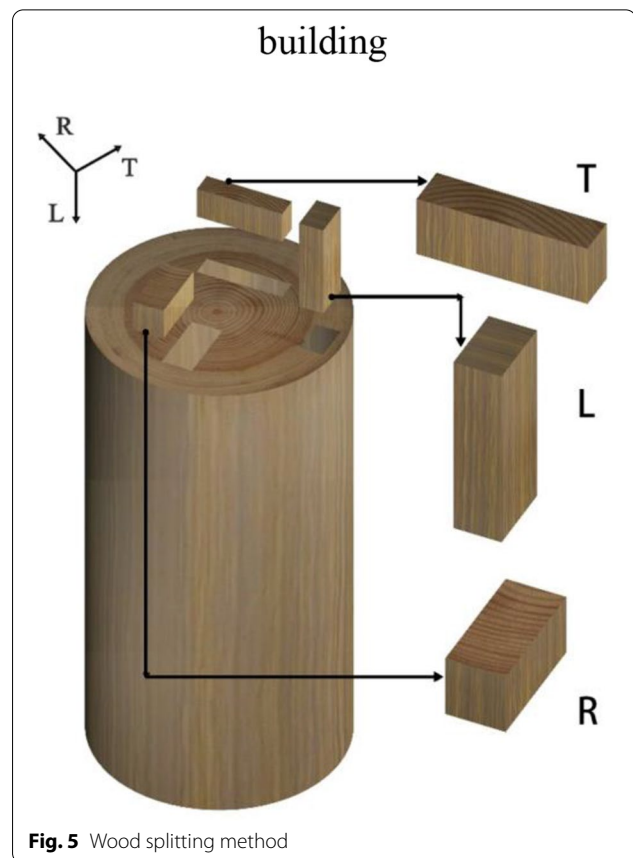

Fig. 5 Wood splitting method

parallel to grains; the radial tensile and compressive strength of wood; the tangential tensile and compressive strength of wood; the shear strength of wood in the surface radial and parallel or tangential and parallel to grain; and the shear strength of wood in the surface tangential and radial to grain. The material property tests were carried out using nine groups of samples, and each group contained five repeated samples.

All the test specimens of material property tests and San-dou component tests were cut from the same wood, based on the specification GB/T 1928–2009 [27]. Before the loading process, all samples were kept at 20 °C and 65% relative humidity until the moisture content reached 12%$\pm$1%. The size of compressed specimens is presented in Fig. 6a, according to GB/T 1935–2009 [28] and GB/T 1943–2009 [29]. The tensile specimen size was determined according to Yoshihara and Ohta's suggestions [30], as shown in Fig. 6b. A pure shear stress state can be created by applying an asymmetric four-point concentrated load on the theoretical fracture surface of the sample under test. Therefore, as shown in Fig. 6c, the mechanical shear parameters were determined according to the Iosipescu shear test method [31, 32]. The CMT 5504 universal testing machine (Mechanical Testing

(a) Tensile test device (b) Compressive test device (c) Shear test device

(d) Tensile failure mode (e) Compressive failure mode (f) Shear failure mode

(g) Tensile specimen size (h) Compressive specimen size (i) Shear specimen size

Fig. 6 Wood property tests (unit: 10^{-3} m)

Zhang *et al. Journal of Wood Science*   (2022) 68:41

Page 7 of 18

& Simulation(MTS) System Corporation, Eden Prairie, United States) with a load capacity of 100 kN was for the determination of the material property, as given in Fig. 6d–f. The mechanical assessment of specimens was performed using a displacement-controlled loading method with a loading rate of 1.0 mm/min. The typical failure modes of specimens are shown in Fig. 6g–i, and the test results are shown in Table 1. As shown in Table 1, the parallel, radial, and tangential directions are represented with L, R, and T notations, respectively. Mechanical properties such as elastic modulus (E), Poisson's ratio (ν), shear modulus (G), tensile strength (f_t), compressive yield strength (f_{cy}), shear strength (f_{LR}, f_{LT} and f_{RT}) were directly obtained by strain gauges placed on the specimens in the material properties test.

Test of lateral push resistance

San-Dou components lateral push resistance tests were performed on four basic sample groups: fir SDPP, fir SDPL, larch SDPP, and larch SDPL, and six samples were tested for each test group. The dimensions of San-dou component were determined according to '*Yingzaofashi*' [33], and the size of SDPP and SDPL were determined to be the same (Fig. 7). An overview of the prepared specimens is presented in Fig. 8.

During the test, the indoor temperature was maintained at about 23 °C, and the specimens were cured to about 11–13% moisture content. The test setup of the performed test is given in Fig. 9. A timber beam was placed on top of the San-dou component, and a horizontal actuator was placed in the middle of the upper edge of the timber beam to apply the eccentric horizontal load. A pre-guided steel plate was mounted on the timber beam

Table 1 Test results of timber

Larch			Fir		
$E_L(10^6\,Pa)$	$E_R(10^6\,Pa)$	$E_T(10^6\,Pa)$	$E_L(10^6\,Pa)$	$E_R(10^6\,Pa)$	$E_T(10^6\,Pa)$
14,870 (7.04)	1318 (4.39)	866 (8.67)	11,563 (5.78)	896 (5.37)	676 (4.63)
$G_{LR}(10^6\,Pa)$	$G_{LT}(10^6\,Pa)$	$G_{RT}(10^6\,Pa)$	$G_{LR}(10^6\,Pa)$	$G_{LT}(10^6\,Pa)$	$G_{RT}(10^6\,Pa)$
1102 (4.76)	872 (8.72)	79 (5.17)	759 (4.95)	650 (3.94)	60 (7.42)
$f_{cyL}(10^6\,Pa)$	$f_{cyR}(10^6\,Pa)$	$f_{cyT}(10^6\,Pa)$	$f_{cyL}(10^6\,Pa)$	$f_{cyR}(10^6\,Pa)$	$f_{cyT}(10^6\,Pa)$
38.3 (5.66)	10.7 (4.86)	8.96 (3.29)	27 (3.94)	5.2 (6.98)	5.0 (2.28)
ν_{LR}	ν_{TL}	ν_{RT}	ν_{LR}	ν_{TL}	ν_{RT}
0.42 (6.65)	0.028 (6.44)	0.62 (4.59)	0.35 (3.42)	0.023 (1.96)	0.43 (6.01)
$f_{tL}(10^6\,Pa)$	$f_{tR}(10^6\,Pa)$	$f_{tT}(10^6\,Pa)$	$f_{tL}(10^6\,Pa)$	$f_{tR}(10^6\,Pa)$	$f_{tT}(10^6\,Pa)$
30.1 (5.27)	3.53 (7.66)	2.93 (5.64)	27 (4.53)	2.12 (2.87)	1.36 (3.01)
$f_{LR}(10^6\,Pa)$	$f_{LT}(10^6\,Pa)$	$f_{RT}(10^6\,Pa)$	$f_{LR}(10^6\,Pa)$	$f_{LT}(10^6\,Pa)$	$f_{RT}(10^6\,Pa)$
10.3 (5.93)	10.71 (7.74)	2.3 (7.35)	6.2 (1.31)	6.1 (1.76)	0.66 (6.18)

Coefficient of variation in parentheses, unit: %, where L represents the parallel direction, R represents the radial direction, and T represents the tangential direction
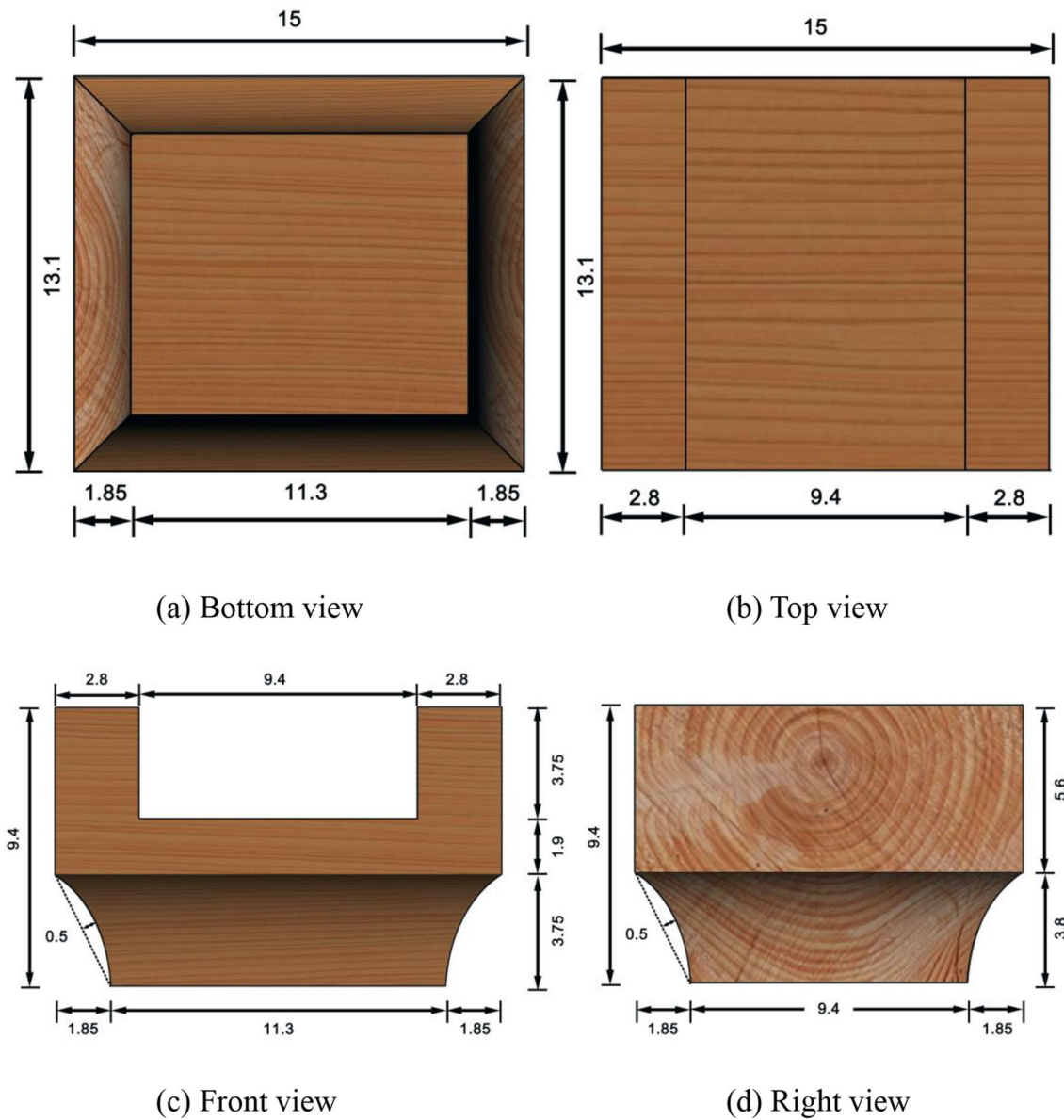
to transfer the upper load and convert it into vertical uniform force. In addition, during the testing, a balanced weight of 400 N was placed on the steel plate to simulate the uniform vertical load from the upper part of the San-dou component. The test procedure was performed by applying a horizontal displacement load with a loading rate of approximately 0.5 mm/min, and the loading process was stopped as the specimens failed. In this paper, the failure of the specimens can be defined as the mode in which the displacement of the loading point increase, and the load measured will decrease rapidly. The jack load, San-dou component displacement, and the typical Dou-ear fracture pattern were all recorded throughout the tests.

Test results and discussion

Typical failure mode

The observation angles of the specimens were rotated 90°, as presented in Fig. 10, to make crack propagation easier to observe. The typical failure mode of both fir and larch in SDPP specimens was the formation of the approximately horizontal cracks on the Dou-ear, resulting in a reduction of overall lateral bearing capacity, as shown in Fig. 10a and b. On the other hand, for the SDPL specimens, the oblique cracks were detected on the Dou-ear for the fir specimen. Oblique cracks propagating from the inside of the Dou-ear to the upper edge of the lower part of the San-dou component eventually caused the Dou-ear to separate from the San-dou component (Fig. 10c). The reason behind this was that under the action of lateral force, the tensile/compressive/shear strengths of wood parallel to the grain were significantly greater than those of wood perpendicular to the grain, as shown in Table 1. These findings indicate that the timber fiber parallel to the grain is generally not easy to break. The phenomenon in such cases is the dislocation between the timber fibers and then the formation of approximately radial cracks in the cross-section (i.e., perpendicular to the annual ring). However, an approximate vertical relationship between crack direction and annual ring direction for larch specimens could not be established (Fig. 10d). This phenomenon can be attributed to the difference in mechanical properties between the two directions perpendicular to the fir grain is quite larger than that of larch(Table 1).

Load–displacement curve

The load–displacement curves of each group of specimens are demonstrated in Fig. 11, and the bearing capacity is given in Table 2. L-S means larch SDPP specimens, L-P means larch SDPL specimens, F-S means fir SDPP specimens, F-P means fir SDPL, and number means the sequence number of repeat group. In general, no

Zhang *et al. Journal of Wood Science*　　(2022) 68:41

Page 8 of 18

Fig. 7 San-dou component size diagram (unit:10^{-2} m)

high level of inconsistency was observed for each group except that L-S-5 and F-P-4 failed at the lower load levels, which means that the data obtained from the tests could be used for the following analysis about the ultimate bearing capacity (Fig. 11). The premature failure in the note of Table 2 means that the ultimate load is 15% less than the mean value. The load–displacement curves of SDPP and SDPL samples showed essentially the same behavior in the region of increasing load: At the first, the specimens had an apparent linear elastic stage. Following that, larch and fir specimens exhibited the plastic hardening at the approximately 500 N load until

their ultimate bearing capacity was reached. Finally, the sample was damaged and exhibited softening behavior. In general, for SDPP samples, when the load reached the ultimate load levels, brittle fracture occurred, and the bearing capacity of the sample was rapidly reduced. However, for SDPL samples, once the ultimate load was reached, the load dropped immediately and could be held at more than 60% of the bearing capacity in a certain loading time, and eventually, the sample was completely damaged. The fir specimen exhibited a gradual softening behavior up to about 80% of its bearing capacity, after which final cracking occurred. The reason for
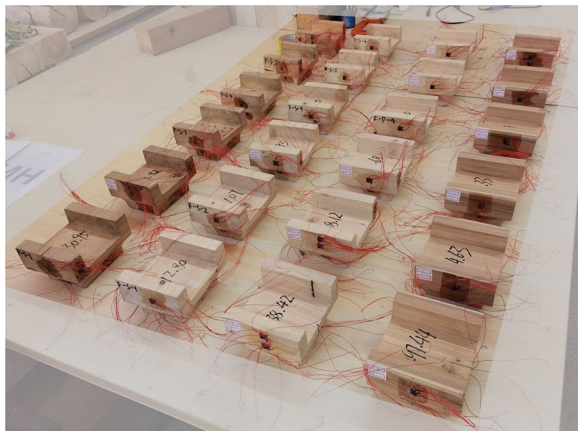
Zhang *et al. Journal of Wood Science* (2022) 68:41

Page 9 of 18

Fig. 8 San-dou specimens

this difference can be demonstrated in Fig. 10c, d, in which the larch specimen exhibited multi-stage cracking during the failure process; however, the fir specimen occurred timber fiber dislocation gradually. It should be noted that there are apparent differences in the part where the load decreases for each sample group due to the different splitting methods of the samples.

Furthermore, the bearing capacity of the larch specimens showed higher performance in the range of 49.64–55.78% compared to the fir specimens with the same size and specimen type (SDPP or SDPL) (Table 2). Besides, for the same size and tree species, SDPP's bearing capacity was 32.85–38.22% higher than SDPL.

Nonlinear evaluation model

Although the dimension of the San-dou component was small, it can be seen from the test phenomenon in the previous section that it had a variety of cracking directions under the action of lateral push force. Then, a simple estimation can be carried out using failure area obtained from Fig. 10 multiplied by the shear strength obtained from Table 1. The estimation results show that the calculation bearing capacities of Fir SDPP, Larch SDPP, Fir SDPL, Larch SDPL are 24,208 N, 37,780 N, 2746 N, and 12,131 N, respectively. These calculation results are very different from those in Table 2, which means the San-dou components are not bearing the pure shear stress but the complex stress. Furthermore, the San-dou component is merely a part of the Dou-gong system, which serves as a load transfer system in practical engineering. Therefore, it is difficult to predict the damage development and stiffness degradation process using the traditional linear analysis model, which makes it challenging to accurately reflect the effect of San-dou component in the Dou-gong system. Hence, it is necessary to develop a nonlinear evaluation model to serve as a foundation for further research into Dou-gong system. The nonlinear study was performed using ANSYS (version 19.0) finite-element software to obtain the mechanical properties of the San-dou specimens. For a San-dou model, the solid185 element was employed to simulate the mechanical behavior of timber, and 40,334 elements were created. Besides, the conta174 and targe170 elements were used to simulate the contact behavior between the timber beam and the San-dou component, and the friction coefficient was 0.4
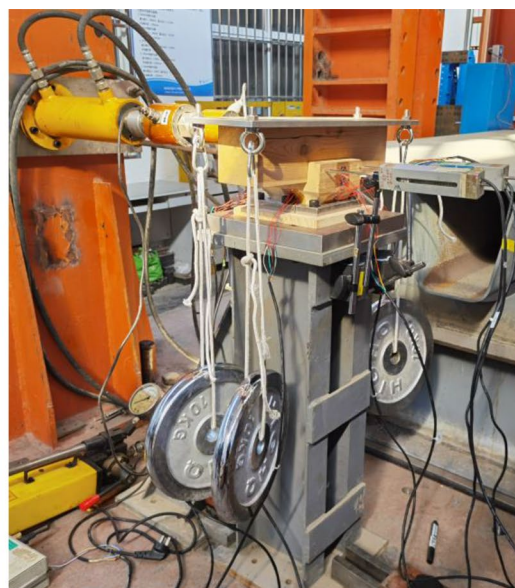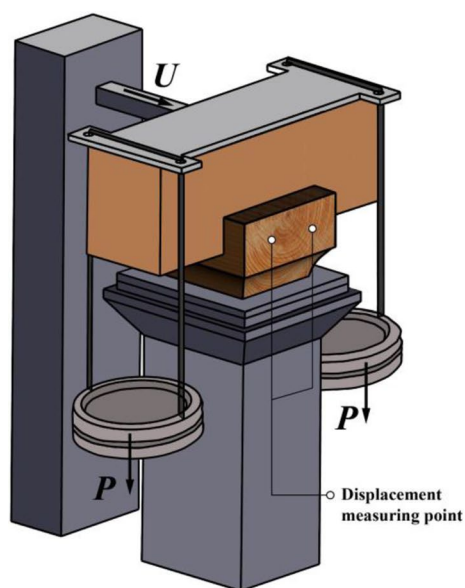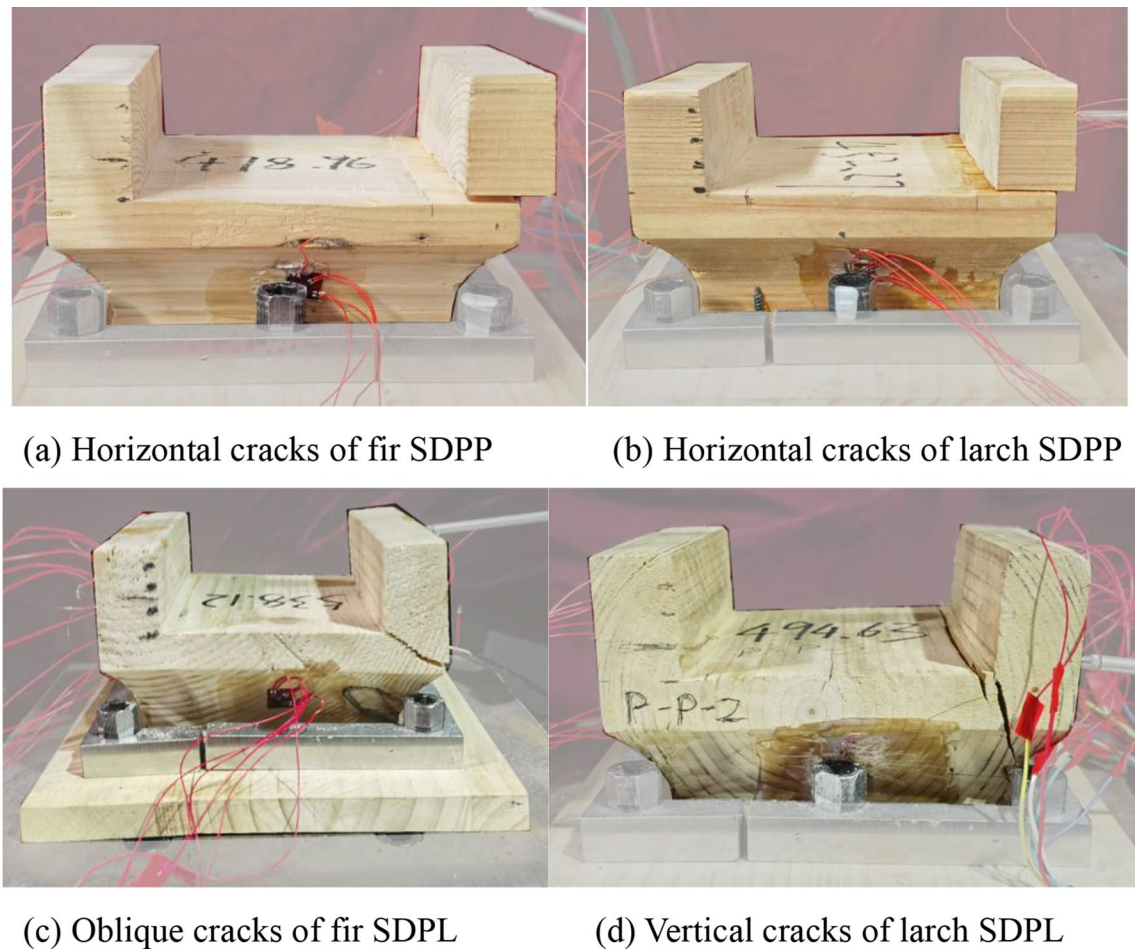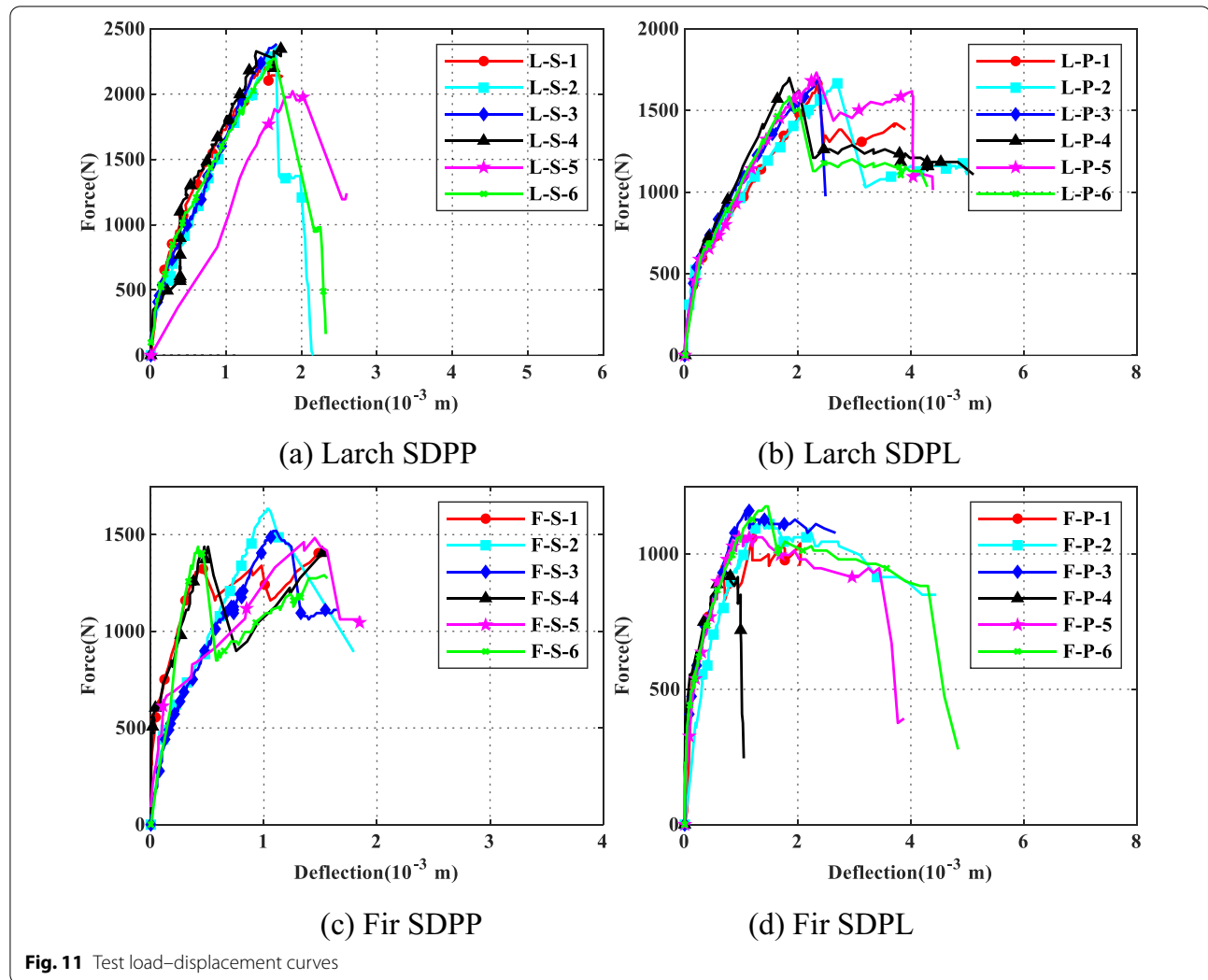

Fig. 9 Overview of the test setup

Zhang *et al. Journal of Wood Science*   (2022) 68:41

Page 10 of 18

Fig. 10 Typical failure modes of SDPP and SDPL

Table 2 Test results of lateral bearing capacity

Numbering	Ultimate load (N)	Mean value (N)	Numbering	Ultimate load (N)	Mean value (N)
L-P-1	1663	1677 (2.73)	L-S-1	2222	2318 (2.68)
L-P-2	1682		L-S-2	2368	
L-P-3	1699		L-S-3	2385	
L-P-4	1700		L-S-4	2346	
L-P-5	1731		L-S-5	/	
L-P-6	1585		L-S-6	2270	
F-P-1	1059	1120 (4.44)	F-S-1	1421	1488 (4.88)
F-P-2	1143		F-S-2	1633	
F-P-3	1160		F-S-3	1519	
F-P-4	/		F-S-4	1437	
F-P-5	1062		F-S-5	1483	
F-P-6	1176		F-S-6	1437	

The brackets in the table are coefficient of variation, unit: %

Symbol '/' represents premature failure of components

The premature failure means the ultimate load is 15% less than the mean value

Zhang *et al. Journal of Wood Science*   (2022) 68:41

Page 11 of 18

Fig. 11 Test load–displacement curves

[4, 5, 26]. The finite-element model of San-dou is shown in Fig. 12.

Timber is an orthotropic material characterized by brittle tensile failure, and tensile strength parallel to the grain is greater than the tensile strength perpendicular to the grain. Compression parallel to grain displays plasticity and damage softening behavior, and during bearing perpendicular to the grain, compression may exhibit a secondary hardening phenomenon [26]. Therefore, the nonlinear material model for timber was generated under the framework of an elastic–plastic damage model, as mentioned in the literature [19]. The model was constructed in ANSYS based on the Fortran language to secondary development in Usermat. The material model's analysis framework adopts an implicit analysis method characterized by a stress–strain relationship, plastic model, damage model, and consistent tangent matrix. The algorithm flowchart is depicted in Fig. 13.

Stress–strain relationship with viscosity regularization

The second-order tensor of total strain ε can be decoupled, as shown in the following equation:

$$\varepsilon = \varepsilon_e + \varepsilon_p \tag{1}$$

where ε_e is a second-order tensor of elastic strain and ε_p is a second-order tensor of plastic strain.

The second-order tensor Cauchy stress σ is used to describe the real stress, and the second-order tensor effective stress $\overline{\sigma}$ is used to describe the stress caused by the elastic strain under the action of the undamaged stiffness matrix. As illustrated in Eq. (2), $\overline{\sigma}$ can be utilized to identify the position of the stress state in plastic space and damage space:

$$\overline{\sigma} = C(d = 0) : \varepsilon_e \quad \sigma = C(d) : \varepsilon_e \tag{2}$$

Zhang *et al. Journal of Wood Science*   (2022) 68:41
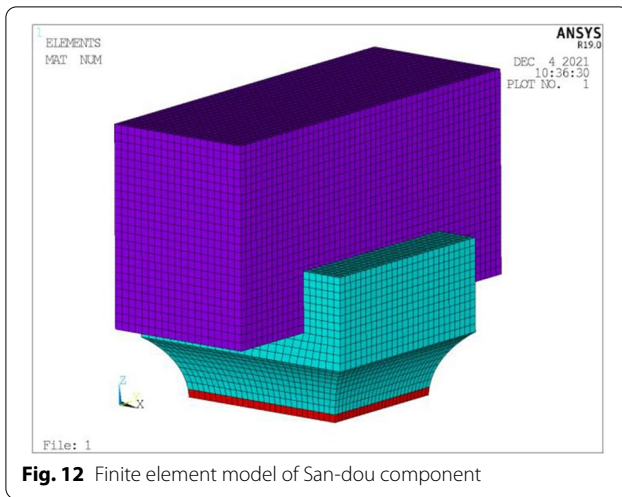
Page 12 of 18

Fig. 12 Finite element model of San-dou component

where the fourth-order tensor $C(d)$ is the damage stiffness tensor, which can adopt Voigt's notation [34]:

where C_{ij} is the orthogonal anisotropic stiffness elastic parameter. Besides d_L, d_R, and d_T are damage variables of parallel, radial, and tangential to grain, respectively. As previously stated, timber has different tensile and compressive properties [35]. Furthermore, because damage softening behavior can lead to numerical solution non-convergence, the viscosity regularization correction approach proposed by Duvaut, Lions [36], and Wang et al. [19] was adopted in this paper to express the damage d_i as in the following equation:

$$(d_i^{n+1})^{\mathrm{v}} = \begin{cases} \frac{\eta}{\eta+\Delta T}(d_{t,i}^n)^{\mathrm{v}} + \frac{\Delta T}{\eta+\Delta T}d_{t,i}^{n+1} & \text{if } \overline{\sigma}_i \geq 0 \\ \frac{\eta}{\eta+\Delta T}(d_{c,i}^n)^{\mathrm{v}} + \frac{\Delta T}{\eta+\Delta T}d_{c,i}^{n+1} & \text{if } \overline{\sigma}_i \leq 0 \end{cases} \quad i = \text{L, R, T}$$

(3)

where subscript c represents compression, t represents tensile, and n represents the n-th step of the implicit

$$C(d) = \begin{bmatrix} (1-d_L)C_{11} & (1-d_L)(1-d_R)C_{12} & (1-d_L)(1-d_T)C_{13} & 0 & 0 & 0 \\ (1-d_L)(1-d_R)C_{21} & (1-d_R)C_{22} & (1-d_R)(1-d_T)C_{23} & 0 & 0 & 0 \\ (1-d_L)(1-d_T)C_{31} & (1-d_R)(1-d_T)C_{32} & (1-d_T)C_{33} & 0 & 0 & 0 \\ 0 & 0 & 0 & (1-d_L)(1-d_R)C_{44} & 0 & 0 \\ 0 & 0 & 0 & 0 & (1-d_L)(1-d_T)C_{55} & 0 \\ 0 & 0 & 0 & 0 & 0 & (1-d_R)(1-d_T)C_{66} \end{bmatrix}$$
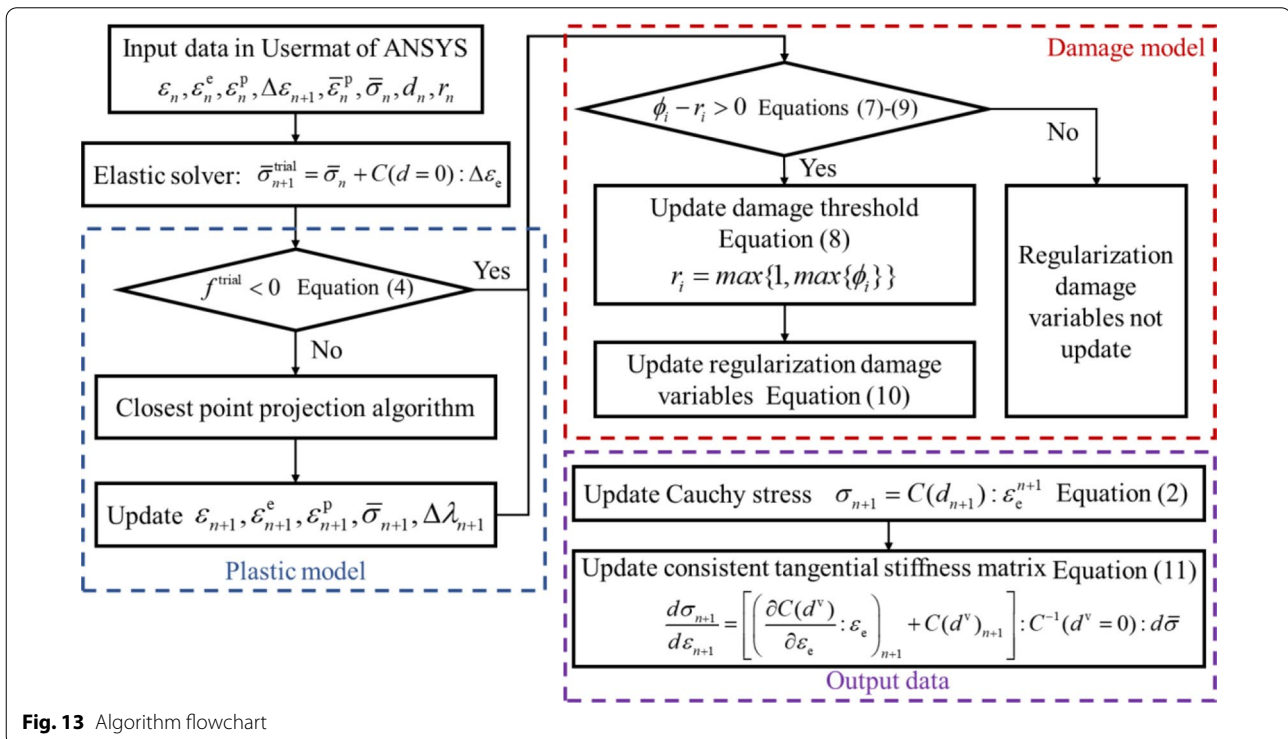

Fig. 13 Algorithm flowchart

solution. In addition, ΔT represents the virtual time interval (controlled by substeps) in the solving process, and η represents the viscosity regularization coefficient which is 0.001.

Plastic model

The plastic model is generally specified by the yield criterion, flow rule and hardening criterion. In this paper, the Hill yield criterion [37] was applied to simulate the orthogonal anisotropy of wood. The yield function satisfying the Kuhn-Tucker condition is shown in in the following equation:

$$f = \sqrt{\sigma^T : H : \sigma^T} - \overline{\sigma}^T_{H\text{-iso}} \tag{4}$$

where $\overline{\sigma}^T_{H\text{-iso}}$ is the isotropic hardening equivalent effective stress and Matrix H is the Hill criterion anisotropic matrix:

$$H = \begin{bmatrix} \frac{(f_0)^2}{(f_{yL})^2} & \frac{(f_0)^2}{2(f_{yT})^2} - \frac{(f_0)^2}{2(f_{yL})^2} - \frac{(f_0)^2}{2(f_{yR})^2} & \frac{(f_0)^2}{2(f_{yR})^2} - \frac{(f_0)^2}{2(f_{yL})^2} - \frac{(f_0)^2}{2(f_{yT})^2} \\ \frac{(f_0)^2}{2(f_{yT})^2} - \frac{(f_0)^2}{2(f_{yL})^2} - \frac{(f_0)^2}{2(f_{yR})^2} & \left(\frac{f_0}{f_{yR}}\right)^2 & \frac{(f_0)^2}{2(f_{yL})^2} - \frac{(f_0)^2}{2(f_{yR})^2} - \frac{(f_0)^2}{2(f_{yT})^2} \\ \frac{(f_0)^2}{2(f_{yR})^2} - \frac{(f_0)^2}{2(f_{yL})^2} - \frac{(f_0)^2}{2(f_{yT})^2} & \frac{(f_0)^2}{2(f_{yL})^2} - \frac{(f_0)^2}{2(f_{yR})^2} - \frac{(f_0)^2}{2(f_{yT})^2} & \left(\frac{f_0}{f_{yT}}\right)^2 \\ & & & \left(\frac{f_0}{f_{LR}}\right)^2 \\ & & & & \left(\frac{f_0}{f_{RT}}\right)^2 \\ & & & & & \left(\frac{f_0}{f_{LT}}\right)^2 \end{bmatrix}$$

where f_0 is the reference stress value, which can be considered as the strength value in the L direction. The meaning of notation about the material parameter is the same as defined in "Timber" section.

As indicated in Eq. (5), the associated flow rule is employed to define the plastic strain increment:

$$d\varepsilon_p = d\lambda \frac{\partial f}{\partial \overline{\sigma}} \tag{5}$$

where ε_p is the plastic strain increment and $d\lambda$ is the plastic flow multiplier increment.

The hardening behavior of timber takes on the hardening criterion proposed by Voce [38], as shown in in the following equation:

$$\overline{\sigma}^T_{H\text{-iso}} = \overline{\sigma}^T_{0\text{-iso}} + Q(1 - e^{-b\overline{\varepsilon}p}) \tag{6}$$

where $\overline{\sigma}^T_{0\text{-iso}}$ is the yield surface without hardening, which can be obtained by introducing the material parameters into Eq. (4). Q and b are hardening parameters that can be calibrated according to the following

procedure. First, the elastic modulus, compression strength, compression yield strength, and stress–strain curve of the entire compression process are determined using a uniaxial compression test. A portion of data points from the yield stress to the ultimate stress on the stress–strain curve, called the nonlinear quasi-hardening branch, can be selected [19]. This section's elastic strain is computed using the elastic modulus, whereas the plastic strain is determined using Eq. (1). Then, the expression's parameters Q and b can be fitted into Eq. (6). In addition, $\overline{\varepsilon}^p$ is the equivalent plastic strain, which can be calculated by the backward Euler scheme using the closest point projection algorithm. The relevant content has been extensively discussed in the work of Simo, Hughes [39], Wang et al. [19], and Chen, Morozov [35].

Damage model

The damage model can be used to describe the softening behavior of materials. The initial damage threshold, threshold evolution, and damage evolution are the three basic components of the damage model. Due to the complexity of compression softening of timber transverse grains and the weak contribution to the bending behavior of timber beams, only the compression damage parallel to grain was considered based on the suggestions of Wang et al. [19]. The damage threshold expression proposed by Sandhaas [40] was utilized in current study, as shown in the following equation:

$$\overline{\sigma}_L > 0, \; \phi_{t,L} = \frac{\overline{\sigma}_L}{f_{tL}}$$
$$\overline{\sigma}_L \leq 0, \; \phi_{c,L} = -\frac{\overline{\sigma}_L}{f_{tL}}$$
$$\overline{\sigma}_R > 0, \; \phi_{t,R} = \left(\frac{\overline{\sigma}_R}{f_{tR}}\right)^2 + \left(\frac{\overline{\sigma}_{LR}}{f_{LR}}\right)^2 + \left(\frac{\overline{\sigma}_{RT}}{f_{RT}}\right)^2$$
$$\overline{\sigma}_T > 0, \; \phi_{t,T} = \left(\frac{\overline{\sigma}_T}{f_{tT}}\right)^2 + \left(\frac{\overline{\sigma}_{LT}}{f_{LT}}\right)^2 + \left(\frac{\overline{\sigma}_{RT}}{f_{RT}}\right)^2$$
$$\tag{7}$$

where $\overline{\sigma}_L, \overline{\sigma}_R, \overline{\sigma}_T$ represent three normal stress and shear stress components of the second-order tensor $\overline{\sigma}$. The other notations are defined in "Timber" section.

Since the damage of the material is irreversible, updating the damage threshold of the material is also irreversible, which means that the updated damage threshold r_i can be expressed as in the following equation:

$$r_i = \max\{1, \max\{\phi_i\}\} i = \text{tL, tR, tT, cL} \qquad (8)$$

The material is considered to undergo damage in the condition that the effective stress satisfies Eqs. (7)–(9):

$$\phi_i - r_i > 0. \qquad (9)$$

In this paper, regarding continuity and computational stability, the damage evolution model proposed by P. Linde et al. [41] and R. Faria et al. [42] was adopted. The damage variables are given in the following equation:

$$d_{t,i} = 1 - \frac{1}{r_{t,i}} e^{\left[(1-r_{t,i})\frac{L_{ch}(f_{t,i})^2}{E_i G_{t,i}}\right]} \quad i = L, R, T$$

$$d_{c,L} = 1 - \frac{1}{r_{c,L}}(1-A) - A e^{[B(1-r_{c,L})]} \qquad (10)$$

where $G_{t,i}$ is the tensile fracture energy of timber, which can be calibrated by the envelope area of the whole process of the load–displacement curve obtained based on the uniaxial tensile test. In this paper, the values of the tensile fracture energies were determined in the light of the research of Chen et al. [26], and Wang et al. [19]. In finite-element analysis, $L_{ch} = \sqrt[3]{V_e}$, is the element's characteristic length, which can be calculated by the cubic root of the element volume and can be utilized to alleviate the mesh dependence problem in the material's softening stage [43]. A and B are damage parameters, which can be calibrated in the following steps. First, the data points are chosen from the section from ultimate stress to final failure in the stress–strain curve, called the softening branch. Second, by decoupling the uniaxial plastic strain and elastic strain with Eqs. (1) and (6), the effective stress at any point on the curve can be computed. Then, the updated threshold and damage can be solved according to Eqs. (7) and (10) for $d_{c,L}$. The values of A and B can be calibrated after any two points on the curve are selected.

The consistent tangential stiffness matrix

The consistent tangential stiffness matrix $d\sigma_{n+1}/d\varepsilon_{n+1}$ can be utilized to update the strain increment and strain in the $(n+1)$th step of the strain-based implicit technique. In this paper, Eq. (11) for the consistent tangential stiffness matrix can be derived from Eq. (2) [19, 44]:

$$\frac{d\sigma_{n+1}}{d\varepsilon_{n+1}} = \left[\left(\frac{\partial C(d^v)}{\partial \varepsilon_e} : \varepsilon_e\right)_{n+1} + C(d^v)_{n+1}\right] : \\ C^{-1}(d^v = 0) : d\overline{\sigma}. \qquad (11)$$

In the plastic iteration, the effective stress increment can be solved by the plastic consistent tangential stiffness matrix, that is, Eq. (12):

$$d\overline{\sigma} = C^{\text{alg}}_{n+1} : d\varepsilon. \qquad (12)$$

Equation (13) can be obtained by substituting Eq. (11) into Eq. (12):

$$\frac{d\sigma_{n+1}}{d\varepsilon_{n+1}} = \left[\left(\frac{\partial C(d^v)}{\partial \varepsilon_e} : \varepsilon_e\right)_{n+1} + C(d^v)_{n+1}\right] : \\ C^{-1}(d^v = 0) : C^{\text{alg}}_{n+1} \qquad (13)$$

where $C^{-1}(d^v = 0)$ is the undamaged flexibility matrix and $C(d^v)_{n+1}$ is the damage stiffness matrix obtained after viscosity regularization correction at the $(n+1)$th substep, which can be solved by Eqs. (2) and (3). According to the suggestion of Chen et al. [44], C^{alg}_{n+1} can be stated by the following equation:

$$C^{\text{alg}}_{n+1} = C_{n+1} - \frac{\left(C_{n+1} : \frac{\partial f_{n+1}}{\partial \overline{\sigma}_{n+1}}\right) \otimes \left(\frac{\partial f_{n+1}}{\partial \overline{\sigma}_{n+1}} : C_{n+1}\right)}{\frac{\partial f_{n+1}}{\partial \overline{\sigma}_{n+1}} : C_{n+1} : \frac{\partial f_{n+1}}{\partial \overline{\sigma}_{n+1}} - \frac{\partial f_{n+1}}{\partial \overline{\varepsilon}^p_{n+1}}}$$

$$C_{n+1} = C^{-1}(d^v = 0) + \Delta\lambda_{n+1}\frac{\partial^2 f}{\partial \overline{\sigma}^2_{n+1}} \qquad (14)$$

where $\Delta\lambda_{n+1}$ is the updated flow multiplier increment obtained by the backward Euler method in the $(n+1)$th substep plastic solution. Then, there is only one unknown quantity $\left(\frac{\partial C(d^v)}{\partial \varepsilon_e} : \varepsilon_e\right)_{n+1}$ in Eq. (13), which can be stated as Eq. (15) by the indicial form:

$$(J_{ij})_{n+1} = \left(\frac{\partial C(d^v)_{ik}\varepsilon_{e,k}}{\partial \varepsilon_{e,j}}\right)_{n+1} \\ = \left(\varepsilon_{e,k}\frac{\partial C(d^v)_{ik}}{\partial d_\alpha}\frac{\partial d_\alpha}{\partial r_\beta}\frac{\partial r_\beta}{\partial \phi_\beta}\frac{\partial \phi_\beta}{\partial \overline{\sigma}_\xi}\frac{\partial \overline{\sigma}_\xi}{\partial \varepsilon_{e,j}}\right)_{n+1} \qquad (15)$$

where i, j, $k, \xi = [1–6]$, $\alpha, \beta = [1–3]$, respectively. Matrix $(J_{ij})_{n+1}$ is an asymmetric matrix, which needs to be solved by the asymmetric Newton method.

Model validation
Damage distribution pattern
The damage distribution indicates the distribution of the stiffness contribution loss during the stress process of the specimen. The calculated damage distribution of
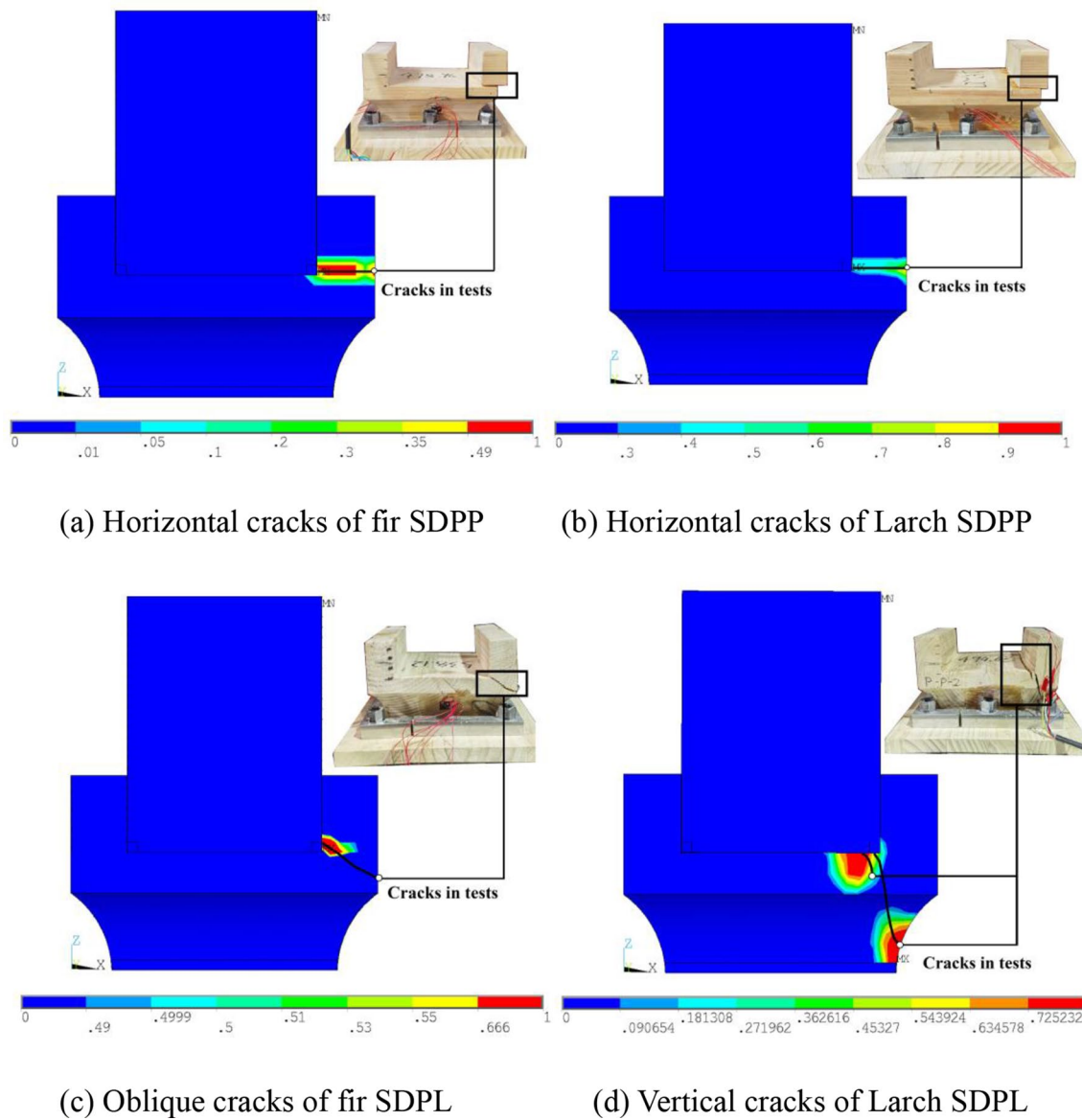
(a) Horizontal cracks of fir SDPP

(b) Horizontal cracks of Larch SDPP

(c) Oblique cracks of fir SDPL

(d) Vertical cracks of Larch SDPL

Fig.14 Damage models

each specimen is shown in Fig. 14. The larger the damage index (red area) is, the more prone the region is to macrocracks. Note that the observation angles of the specimens were rotated 90 degrees in Fig. 14 to make crack propagation easier to observe. The damage distribution cloud trend generated by the assessment model in this research was consistent with the crack direction determined by the test, as shown in Fig. 14. Therefore, the damage model used in this paper can be considered to meet the accuracy requirements.

Load–displacement curve

The calculated load–displacement curve is plotted in Fig. 15 and the calculated ultimate bearing capacity is recorded in Table 3. The overall trend of the load–displacement curve is close to the experimental results due to the consideration of damage and plasticity, as demonstrated in Fig. 15. In particular, the rising part of the load–displacement curve in Fig. 15d is similar to the test results; however, the ductility of the descending part is lower than the test results. That is because, in the process
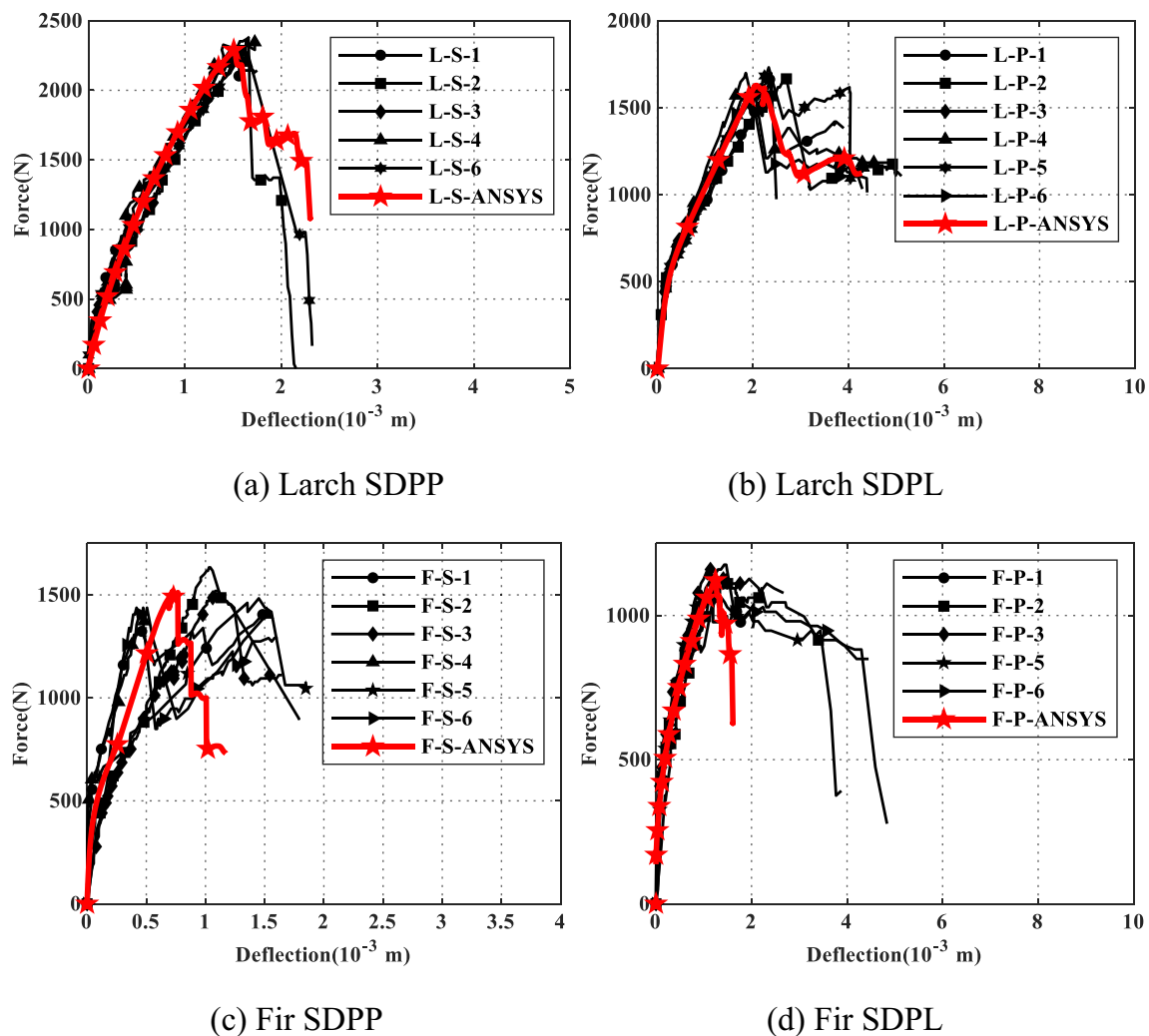
Zhang *et al. Journal of Wood Science* (2022) 68:41

Page 16 of 18

Fig.15 Calculation results of load–displacement curve

Table 3 Comparison of finite-element analysis and test results

Name of specimens	Test results (N)	Calculated results (N)	Calculated errors (%)
Larch SDPL	1677	1628	− 2.92
Fir SDPL	1120	1123	0.27
Larch SDPP	2318	2291	− 1.16
Fir SDPP	1488	1519	2.08

of the numerical analysis, the actual wood softening process was simplified. According to Eq. (10), the softening stage is assumed as a given function. However, the actual softening stage of wood is very complex and creates an intense uncertainty. This shortcoming of the method needs to be discussed in further study.

Table 3 reveals that the bearing capacity error between finite-element analysis and test results is in the range of − 2.92 to 2.08%, indicating that the evaluation method suggested in this research can accurately assess the bearing capacity of SDPP and SDPL.

Conclusions

SDPP and SDPL are two varieties of San-dou components that widely exist in traditional East Asian timber constructions. However, they are vulnerable to the lateral push force from the Gong, beam and purlin. Therefore, the structural performance of SDPP and SDPL was analyzed through tests and finite-element analysis to evaluate the lateral push resistance of these two San-dou component types. First, the material properties of larch and fir were tested to obtain the material parameters

Zhang *et al. Journal of Wood Science* (2022) 68:41

Page 17 of 18

that would be employed in numerical simulation. Then, 24 San-dou specimens were produced to investigate the effect of SDPP and SDPL on lateral push resistance. Finally, the SDPP and SDPL evaluation models are developed using the elastic–plastic damage model. In this paper, the following conclusions can be drawn.

(1) In the lateral push resistance test, the failure mode has a typical law: for the SDPL, the failure mode is a horizontal crack parallel to the Dou-ear. For fir SDPP, the mode of failure is an oblique crack perpendicular to the annual ring extending from the inner edge of the Dou-ear to the upper edge of the lower part of the San-dou component. The failure mode of the larch SDPP is similar to that of the fir one, except that the crack direction is not perpendicular to the annual ring, and the crack is from the inner edge of Dou-ear to the bottom of the specimen.

(2) The lateral push resistance of San-dou components is heavily influenced by the timber species and timber splitting method. Under the same conditions, the bearing capacity of larch San-dou component is stronger than that of fir San-dou component, with an increment of 49.64–55.78%. The bearing capacity of the SDPP is generally higher than that of the SDPL, with an increment of 32.85–38.22%.

(3) The orthogonal anisotropic elastic–plastic damage model used in this paper can accurately simulate these two types of San-dou components (SDPL and SDPP) in the traditional timber building. The error between the calculated bearing capacity and the test results is between -2.92–2.08%. In addition, the load–displacement curves and damage distribution modes are also highly close to the test results.

However, it should be emphasized that Dou-gong is a complicated timber structure system widely used in East Asia. Moreover, San-dou components in traditional Chinese timber buildings differ slightly from those in traditional Japanese timber buildings and traditional South Korean timber buildings in terms of architectural form, wood material, and construction technique, which need further research. The conclusions obtained in this paper can be directly used to reveal the structural performance of Chinese San-dou components and provide relevant research methodologies and foundations for those of other East Asian countries. Furthermore, the effect of the pith position on the lateral push resistance of San-dou component was not considered in the current study; however, this can be investigated in future research.

Abbreviations
SDPP: San-dou component perpendicular to the grain; SDPL: San-dou component parallel to the grain.

Author contributions
CZ contributed to the methodology, simulation, results analysis, and original draft of this manuscript. QC contributed to the review of this manuscript. All authors contributed to the scanning and surveying of the temple. All authors read and approved the final manuscript.

Availability of data and materials
The datasets used and/or analysed during the current study are available from the corresponding author on reasonable request.

Declarations

Competing interests
The authors declare that they have no competing interests.

References
1. Chen Z, Zhu E, Lam F, Pan J (2014) Structural performance of Dou-Gong brackets of Yingxian Wood Pagoda under vertical load—an experimental study. Eng Struct 80:274–288. https://doi.org/10.1016/j.engstruct.2014.09.013
2. Zhang CW, Chun Q, Lin YJ, Han YD, Jia XH (2021) Quantitative assessment method of structural safety for complex timber structures with decay diseases. J Build Eng. https://doi.org/10.1016/j.jobe.2021.103355
3. Shiqing Z (2012) Form and meaning of the wood-grain of the Dou in Dougong bracket-analysis of the crosscut Dou in the main hall of Baoguo temple. Cult Relics 9:74–80. https://doi.org/10.13619/j.cnki.cn11-1532/k.2012.09.005 (**in Chinese**)
4. Fujita K (2019) Dynamic performance of bracket complexes used in traditional timber structures in Japan. Proc Jpn Acad Ser B Phys Biol Sci 95(9):568–580. https://doi.org/10.2183/pjab.95.038
5. Xie Q, Wang L, Zhang L, Xiang W, Hu W (2020) Rotational behaviors of fork-column Dou-Gong: experimental tests and hysteresis model. J Perform Constr Facil. https://doi.org/10.1061/(asce)cf.1943-5509.0001426
6. Zhiyong C (2011) Behaviour of typical joints and the structure of YingXian Wood Pagoda. Dissertation, Harbin Institute of Technology. https://kns.cnki.net/KCMS/detail/detail.aspx?dbname=CDFD1214&filename=1012024162.nh (**in Chinese**) Accessed June 8 2022.
7. Wu C, Xue J, Song D, Ren G, Zhang J (2022) Mechanical performance of inclined Dougong bracket sets under vertical load: experimental tests and finite element calculation. J Build Eng 45:103555. https://doi.org/10.1016/j.jobe.2021.103555
8. Miao Z (2020) The wood grain and shape of the Dou components in North China during Tang and Song Dynasties. Inter Des Constr 5:136–137 (**in Chinese**)
9. Cha J-H, Kim Y-J (2021) Rethinking the proportional design principles of timber-framed buddhist buildings in the Goryeo era. Religions. https://doi.org/10.3390/rel12110985
10. Foley C (2001) A three-dimensional paradigm of fiber orientation in timber. Wood Sci Technol 35(5):453–465. https://doi.org/10.1007/s0022601001 12

Zhang *et al. Journal of Wood Science*   (2022) 68:41

Page 18 of 18

11. Rjasanowa K, Rösch R (1995) Baumstammodelle zur Simulation von Holz-maserungen. Holz als Roh-und Werkstoff 53(4):221–224 (**(in German)**)

12. Diaz-Maroto IJ, Tahir S (2018) Testing of wood physical properties in oak species (*Quercus Robur* L., *Q. Petraea*(Matts) Liebl. and *Q. Pyrenaica* Willd.) for cooperage. Part II: wood grain. Wood Res 63(6):959–969

13. "Technical code for maintenance and strength ening of ancient timber buildings" editorial team (1994) Investigation of tree species for wood structures of ancient buildings and analysis of the main properties. Sichuan Build Sci 1:11–14 (**in Chinese**)

14. Fujita K, Sakamoto I, Ohashi Y (2000) Static and dynamic loading tests of bracket complexes used in traditional timber structures in Japan. In: 12th World Conference on Earthquake Engineering, Auckland, New Zealand, 30 January–4 February 2000. Wellington; New Zealand Society for Earth-quake Engineering

15. Fujita K, Kimura M, Ohashi Y, Sakamoto I (2001) Hysteresis model and stiffness evaluation of bracket complexes used in traditional timber structures based on static lateral loading tests. J Struct Constr Eng 543:121–127. https://doi.org/10.3130/aijs.66.121_2 (**in Japanese**)

16. Yeo SY, Hsu M-F, Komatsu K, Chung Y-L, Chang W-S (2016) Shaking table test of the Taiwanese traditional Dieh-Dou timber frame. Int J Architect Herit 10(5):539–557. https://doi.org/10.1080/15583058.2015.1009574

17. Yeo SY, Komatsu K, Hsu M-F, Que Z (2016) Mechanical model for complex brackets system of the Taiwanese traditional Dieh-Dou timber structures. Adv Struct Eng 19(1):65–85. https://doi.org/10.1177/1369433215618269

18. Yinlan S, Zaigen M, Schneider J, Stiemer SF (2016) Numerical simulation study and damage analysis of cross laminated timber connections. Chin J Eng 38(1):149–157 (**in Chinese**)

19. Wang M, Song X, Gu X (2018) Three-dimensional combined elastic-plastic and damage model for nonlinear analysis of wood. J Struct Eng. https://doi.org/10.1061/(ASCE)ST.1943-541X.0002098

20. Xue J, Liang X, Wu C, Song D, Qi L (2022) Experimental and numerical study on eccentric compression performance of Dou-Gong brackets at column tops. Structures 35:608–621. https://doi.org/10.1016/j.istruc.2021.11.035

21. Qin S, Yang N (2018) Strength degradation and service life prediction of timber in ancient Tibetan building. Eur J Wood Wood Prod 76(2):731–747. https://doi.org/10.1007/s00107-017-1211-x

22. Yang N, Zhang L (2018) Investigation of elastic constants and ultimate strengths of Korean pine from compression and tension tests. J Wood Sci 64(2):85–96. https://doi.org/10.1007/s10086-017-1671-y

23. Nairn JA (2007) A numerical study of the transverse modulus of wood as a function of grain orientation and properties. Holzforschung 61(4):406–413. https://doi.org/10.1515/hf.2007.079

24. Mendis MS, Halwatura RU, Somadeva DRK, Jayasinghe RA, Gunawardana M (2019) Influence of timber grain distribution on orientation of saw cuts during application: reference to heritage structures in Sri Lanka. Case Stud Constr Mater. https://doi.org/10.1016/j.cscm.2019.e00237

25. Guindos P (2016) Method for the integral calculation of the fiber orienta-tion and the fundamental material properties of softwood logs and lum-ber. Holzforschung 70(10):981–991. https://doi.org/10.1515/hf-2015-0197

26. Chen Z, Ni C, Dagenais C, Kuan S (2020) Wood ST : A temperature-dependent plastic-damage constitutive model used for numerical simu-lation of wood-based materials and connections. J Struct Eng. https://doi.org/10.1061/(asce)st.1943-541x.0002524

27. GB/T 1928–2009 (2009) General requirements for physical and mechani-cal tests of wood. General Administration of Quality Supervision IaQotP-sRoC. (in Chinese)

28. GB/T 1935–2009 (2009) Methods of testing in compressive strength parallel to grain of wood. General Administration of Quality Supervision IaQotPsRoC. (in Chinese)

29. GB/T 1943–2009 (2009) Method for determination of the modulus of elasticity in compression perpendicular to grain of wood. General Admin-istration of Quality Supervision IaQotPsRoC. (in Chinese)

30. Yoshihara H, Ohta M (2000) Estimation of the shear strength of wood by uniaxial-tension tests of offaxis specimens. J Wood Sci 46:159–163. https://doi.org/10.1007/BF00777364

31. Yoshihara H, Ohsaki H, Kubojima Y, Ohta M (1999) Applicability of the Iosipescu shear test on the measurement of the shear properties of wood. J Wood Sci 45:24–29. https://doi.org/10.1007/BF00579520

32. Zhang L, Yang N (2017) Evaluation of a modified Iosipescu shear test method for determining the shear properties of clear wood. Wood Sci Technol 51(2):323–343. https://doi.org/10.1007/s00226-016-0888-z

33. Jie L (1954) Ying-tsao-fa-shih. Commercial Press, Shanghai (**in Chinese**)

34. Shigang A, Daining F, Rujie H, Yongmao P (2015) Effect of manufacturing defects on mechanical properties and failure features of 3D orthogonal woven C/C composites. Compos B Eng 71:113–121. https://doi.org/10.1016/j.compositesb.2014.11.003

35. Chen J-F, Morozov EV (2016) A consistency elasto-viscoplastic damage model for progressive failure analysis of composite laminates subjected to various strain rate loadings. Compos Struct 148:224–235. https://doi.org/10.1016/j.compstruct.2016.03.049

36. Duvaut G, Lions JL (2012) Inequalities in mechanics and physics. Springer, Berlin

37. Hill R (1948) A theory of the yielding and plastic flow of anisotropic met-als. Proc R Soc Lond A 193(1033):281–297. https://doi.org/10.1098/rspa.1948.0045

38. Voce E (1948) The relationship between stress and strain for homogene-ous deformation. J Inst Met 74(11):537–562

39. Simo JC, Hughes TJ (2006) Computational inelasticity, vol 7. Springer, Berlin

40. Sandhaas C (2012) Mechanical behaviour of timber joints with slotted-in steel plates., Delft Univ. of Technology, Delft, Netherlands

41. Linde P, Pleitner J, Boer HD, Carmone C (2004) Modelling and simulation of fibre metal laminates. In: ABAQUS Users's Conference, Boston, Mas-sachusetts, 25–27 May, 2004. Dassault Systemes Simulia Corp, Providence

42. Faria R, Oliver J, Cervera M (1998) A strain-based plastic viscous-damage model for massive concrete structures. Int J Solids Struct 35(14):1533–1558. https://doi.org/10.1016/S0020-7683(97)00119-4

43. Bažant ZP, Oh BH (1983) Crack band theory for fracture of concrete. Matériaux Constr 16(3):155–177. https://doi.org/10.1007/BF02486267

44. Chen JF, Morozov EV, Shankar K (2012) A combined elastoplastic damage model for progressive failure analysis of composite materials and struc-tures. Compos Struct. https://doi.org/10.1016/j.compstruct.2012.04.021

Publisher's Note